Theoretical analysis of hard x-ray generation by nonperturbative interaction of ultrashort light pulses with a metal

Jannick Weisshaupt, Vincent Juvé, Marcel Holtz, Michael Woerner,[a)] and Thomas Elsaesser
Max-Born-Institut für Nichtlineare Optik und Kurzzeitspektroskopie, 12489 Berlin, Germany

The interaction of intense femtosecond pulses with metals allows for generating ultrashort hard x-rays. In contrast to plasma theories, tunneling from the target into vacuum is introduced as electron generation step, followed by vacuum acceleration in the laser field and re-entrance into the target to generate characteristic x-rays and Bremsstrahlung. For negligible space charge in vacuum, the Kα flux is proportional to the incident intensity and the wavelength squared, suggesting a strong enhancement of the x-ray flux by mid-infrared driving pulses. This prediction is in quantitative agreement with experiments on femtosecond Cu Kα generation. © *2015 Author(s). All article content, except where otherwise noted, is licensed under a Creative Commons Attribution 3.0 Unported License.* [http://dx.doi.org/10.1063/1.4915485]

I. INTRODUCTION

Non-perturbative light-matter interactions are induced by optical fields which are comparable to or stronger than intraatomic or interionic electric fields, resulting in light-driven coherent electron dynamics on the time scale of the optical cycle, ionization processes, and plasma generation from dense materials.[1–7] Apart from their fundamental relevance for probing nonequilibrium properties of matter, such phenomena have been exploited extensively for generating short-wavelength radiation from the extended ultraviolet (EUV) to the hard x-ray range.[8–21] High-harmonic generation from gaseous targets, which covers the EUV and soft x-ray range, is based on light-induced tunneling of electrons into vacuum, field-driven coherent motion of the free electron, and recombination with the ionized atom.[22] Hard x-ray generation has exploited electrons which are accelerated outside a metal target and produce characteristic x-ray emission and Bremsstrahlung after re-entering it.

Ultrashort hard x-ray pulses have been generated by shining intense optical pulses at visible or near-infrared wavelengths on metallic targets and collecting the characteristic x-rays emitted in backward or forward direction.[1,17,19,21] State-of-the-art femtosecond sources of this type work at up to kilohertz repetition rates with a total x-ray flux of up to 10^{11} photons/s and have found widespread application in time-resolved x-ray diffraction.[4,5,10] For analyzing the generation mechanisms, the following 3 steps are distinguished: (i) provision of free electrons either in a laser-generated plasma at the target or by field-induced extraction from the target (step 1 in Fig. 1), (ii) electron acceleration in the plasma or in the vacuum by the strong laser field (step 2), and (iii) electron re-entrance into the target, collisional inner-shell ionization, and x-ray emission by a radiative transition of an outer-shell electron into the unoccupied inner shell (step 3). This scheme requires a strong electric field component perpendicular to the target surface as exists, e.g., for a p-polarized driving field under a large angle of incidence.

In the laser-plasma scenario, a pre-pulse[23,24] or the leading part of the main pulse creates a very hot ($k_B T \approx 500 \, \text{eV}$) overdense plasma at the surface of the metal target [Fig. 2(a)]. The initial condition for the subsequent electron acceleration (step 2) depends strongly on the
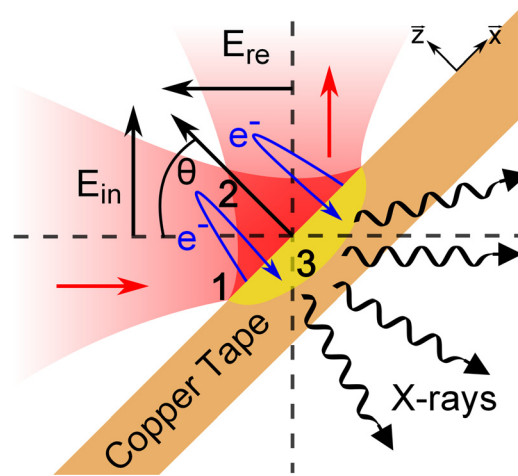
---

a)woerner@mbi-berlin.de

2, 024102-1

FIG. 1. Laser-target interaction geometry and the x-ray generation process. The coordinate system used in our theory is indicated by the vectors $\vec{x}$ and $\vec{z}$.

formation time of the plasma, in particular, for optical driver pulses of sub-50 fs duration. Formation of a thermalized hot plasma with $kT \approx 500\,\mathrm{eV}$ requires inelastic collisions between electrons and ions in the target, processes which are expected to take several hundreds of femtoseconds, i.e., substantially longer than the optical cycle of the driving field.[25,26] This issue has remained unaddressed in most plasma models which use empirical plasma parameters as initial conditions. After creation of the high temperature plasma it starts to expand into vacuum with a low speed. Within 100 fs, copper ions of a thermal energy $k_B T \approx 500\,\mathrm{eV}$ travel only a distance of $\approx 4\,\mathrm{nm}$ which is distinctly less than the skin depth at the driver wavelength. As a consequence plasma expansion effects due to a pre-pulse are relevant on a $\approx 10\,\mathrm{ps}$ time scale.[23,24]
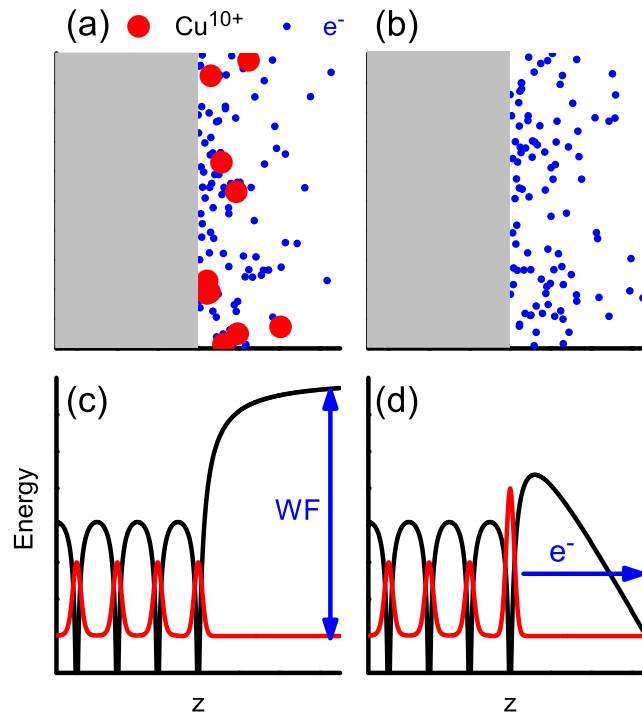

FIG. 2. Basic concepts of different models for hard x-ray generation with femtosecond laser pulses on metal targets. (a) Laser-plasma model. (b) Vacuum heating or "Brunel" model without quantum mechanical effects. (c) and (d) Metal model potentials including the action of the driving field for (c) $E = 0$ and (d) $E > 0$.

A completely different approach pioneered by Brunel[27] considers a one-dimensional capacitor model in which the target at $z = 0$ represents a perfect conductor which can freely emit electrons [Fig. 2(b)]. Using the constraint of classical electrodynamics that the electric field perpendicular to the surface has to vanish at the metal-vacuum interface, the dynamic space-charge in the vacuum determines uniquely the density of electrons which are accelerated in the field and reenter the target. In order to ensure the applicability of Brunel's concept, it is necessary to have a high contrast to pre-pulses to make sure that no plasma has formed before the main pulse arrives.[28] The modern development of the high power femtosecond lasers[29] allows for extremely high contrast ratios down to 10^{-10}. Brunel's concept has been shown to give a realistic description in an intermediate range of field strengths while it fails in the limits of both very small and very high electric fields. At low fields, electrons cannot be extracted from a real metal because of the large triangular barrier determined by the work function (WF) and the applied electric field [Figs. 2(c) and 2(d)]. At very high electric fields, Brunel's model predicts arbitrarily high electron densities in the vacuum $n_{\mathrm{vac}}(z, t) \gg n_{\mathrm{metal}}$ during the field-buildup for the typical fields used in experiments.

In this article, we present a novel theoretical concept for laser-driven femtosecond hard x-ray sources which overcomes the problems discussed above. Our theoretical study focuses on few cycle driving pulses with a pulse duration of $t_p < 100$ fs and high contrast to pre-pulses, so that essentially no plasma has formed before the main pulse arrives. Optimal Kα flux is observed for excursion lengths of the electrons on the order of $\lambda/4$ which are orders of magnitude larger than those of the ions (see estimate above). In such a scenario vacuum heating strongly dominates over resonant absorption.[28] Thus, similar to Brunel's concept[27] we treat the light-metal target interaction with the linear Fresnel equations for electrons residing in the metal and use the vacuum heating model for electrons in the vacuum. For electron extraction from the metal surface, we introduce a quantum mechanical tunneling picture with a barrier width and height modulated by the optical driving field. This keeps the electron charge densities $n_{\mathrm{vac}}(z, t)$ in the vacuum at any time much smaller than in the metal, i.e., $n_{\mathrm{vac}}(z, t) \ll n_{\mathrm{metal}}$. In addition, we include in an effective one-dimensional propagation geometry also the radiation reaction field. The latter allows for radiative damping and ensures energy conservation in the light-matter interaction.

We discuss theoretical results as a function of various parameters such as incident intensity I, driver wavelength λ, angle of incidence θ, and the carrier-envelope phase ϕ_{cep} of the driving pulses. The theoretical predictions agree well with recent experimental results.[18,21] In the case of negligible space charge in the vacuum, our theory predicts an x-ray flux being proportional to the incident intensity and the wavelength squared $I \lambda^2$. This scaling law is relevant for future ultrafast hard x-ray sources driven at mid-infrared wavelengths. For optimized focusing conditions, the space charge enhances the x-ray flux for $\lambda < 3.5 \, \mu$m slightly and causes a gradual saturation for longer wavelengths.

II. THEORETICAL MODEL

In this section, we describe our theoretical model in detail, following the stepwise generation scheme illustrated in Fig. 1.

A. Optical propagation geometry and electron equations of motions

We consider a one-dimensional light propagation geometry to keep the numerical effort limited and get a deeper insight into electron extraction and acceleration (Fig. 1). P-polarized light is focused under the angle of incidence θ onto the metal target, e.g., a copper tape. The incident and reflected waves form a standing wave along the z-coordinate (surface normal of metal). Assuming plane phase fronts of the incident and reflected waves, the effective one-dimensional propagation is described by

$$\vec{E}_{\mathrm{in}}^{\mathrm{3D}}(x, y, z, t) = E_{\mathrm{in}}\left(t - \frac{x}{c}\sin\theta + \frac{z}{c}\cos\theta\right) \begin{pmatrix} \cos\theta \\ 0 \\ \sin\theta \end{pmatrix}, \tag{1}$$

$$\vec{E}_{re}^{3D}(x,y,z,t) = E_{re}\left(t - \frac{x}{c}\sin\theta - \frac{z}{c}\cos\theta\right)\begin{pmatrix} -\cos\theta \\ 0 \\ \sin\theta \end{pmatrix}$$

$$= E_{in}\left(t - \frac{x}{c}\sin\theta - \frac{z}{c}\cos\theta - \frac{\lambda}{2\pi c}\Phi[r_p(\lambda,\theta)]\right)$$

$$\times |r_p(\lambda,\theta)|\begin{pmatrix} -\cos\theta \\ 0 \\ \sin\theta \end{pmatrix}. \tag{2}$$

In Eq. (2), we use the complex Fresnel coefficient for metal reflection $r_p(\lambda, \theta)$ the phase $\Phi[r_p(\lambda, \theta)]$ of which determines its dispersion. The amplitude $|1 + r_p(\lambda, \theta)|\sin\theta$ plotted in Fig. 3(a) shows that the electric fields in the vacuum close to the metal surface point essentially into the z-direction for angles θ close to the respective maximum of the curves. We neglect any influence of the magnetic field on the electron motion, i.e., the vacuum electron motions in the
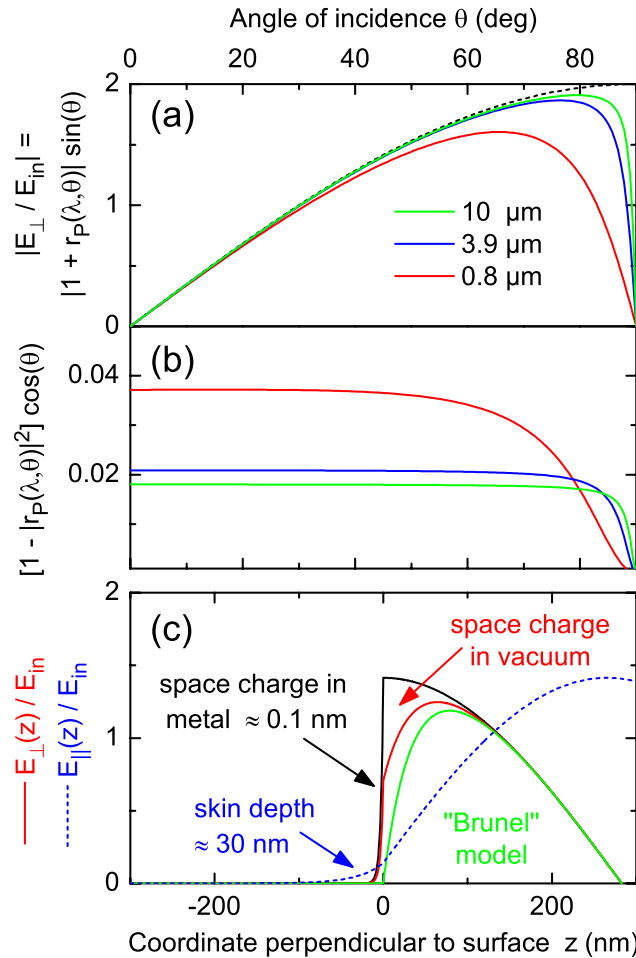

FIG. 3. Electric field at the metal-vacuum interface. (a) Amplitude of the electric field component perpendicular to the surface $E_\perp = E_{in}|1 + r_p(\lambda, \theta)|\sin(\theta)$ as a function of the angle of incidence θ for different driver wavelengths λ (dashed line: ideal conductor). (b) Absorbed laser power per unit area of metal surface normalized to the intensity of the incident beam $[1 - |r_p(\lambda, \theta)|^2]\cos(\theta)$. (c) Electric field distributions $E_\perp(z)$ and $E_\parallel(z)$ along the coordinate z perpendicular to the surface. Red line: $E_\perp(z)$ decays due to both space charge within the metal and that of electrons emitted into the vacuum. The electric field parallel to the surface $E_\parallel(z)$ (blue dashed line) decays in the metal with the skin depth and shows in the vacuum a standing wave out of phase with that of $E_\perp(z)$. Green line: in the "Brunel" model $E_\perp(z)$ vanishes exactly at the metal-vacuum interface $z = 0$. Black line: $E_\perp(z)$ for low fields without electrons in the vacuum.

x- and y-directions. This results in the following expressions for the electric charge in vacuum, i.e., the space charge, and the current of vacuum electrons:

$$n_{\text{vac}}^{\text{3D}}(x,y,z,t) = -\frac{e_0}{A}\Theta(z)\sum_{i=1}^{N}\delta\left[z - z_i\left(t - \frac{x}{c}\sin\theta\right)\right]$$

$$= n_{\text{vac}}\left(z, t - \frac{x}{c}\sin\theta\right), \tag{3}$$

$$\vec{J}_{\text{vac}}^{\text{3D}}(x,y,z,t) = -\frac{e_0}{A}\Theta(z)\begin{pmatrix}0\\0\\1\end{pmatrix}\sum_{i=1}^{N}v_i\left(t - \frac{x}{c}\sin\theta\right)\delta\left[z - z_i\left(t - \frac{x}{c}\sin\theta\right)\right]$$

$$= J_{\text{vac}}\left(z, t - \frac{x}{c}\sin\theta\right)\begin{pmatrix}0\\0\\1\end{pmatrix}, \tag{4}$$

$$v_i = \frac{dz_i}{dt} = \frac{p_i}{\sqrt{m_e^2 + \left(\frac{p_i}{c}\right)^2}}, \tag{5}$$

e_0 is the elementary charge, $\Theta(z)$ the heaviside step-function has a value of 1 for $z > 0$ and 0 for $z < 0$, and A is a normalization area to be determined yet (see below). In our model calculation, we use an ensemble of N electrons with spatial positions z_i and velocities v_i with the relativistic relation (5) to their momenta p_i. To account properly for the local field acting on each electron, one has to include the incident (1) and reflected beam (2) as well as the electric field generated by the charge density (3) and current (4) originating from the electrons in vacuum, i.e., from the space charge. The vacuum electrons emit the radiation reaction field which leads to radiative damping of the electron motion and accounts correctly for energy conservation in the light-matter interaction.

The light propagation geometry used here is identical to our earlier work on radiative coupling effects of inter-subband transitions in semiconductor multiple quantum well samples.[30–32] The retarded Green's function tensor in dyadic form [Eq. (A2) of Ref. 30] provides the electric field re-emitted by electrons in vacuum

$$\vec{E}_{\text{em}}^{\text{3D}}(x,y,z,t) = -\frac{Z_0\tan\theta}{2}\int_0^\infty dz' \times \left\{ J_{\text{vac}}\left(z', t - \frac{x}{c}\sin\theta - \frac{|z - z'|}{c}\cos\theta\right) \right.$$

$$\times \begin{pmatrix}[\Theta(z' - z) - \Theta(z - z')]\cos\theta\\0\\\sin\theta\end{pmatrix}$$

$$\left. + J_{\text{vac}}\left(z', t - \frac{x}{c}\sin\theta - \frac{z + z'}{c}\cos\theta - \frac{\lambda}{2\pi c}\Phi[r_{\text{p}}(\lambda,\theta)]\right)|r_{\text{p}}(\lambda,\theta)|\begin{pmatrix}-\cos\theta\\0\\\sin\theta\end{pmatrix}\right\}$$

$$= E_{\text{em(in)}}\left(z, t - \frac{x}{c}\sin\theta\right)\begin{pmatrix}\cos\theta\\0\\\sin\theta\end{pmatrix} \tag{6}$$

$$+ E_{\text{em(re)}}\left(z, t - \frac{x}{c}\sin\theta\right)\begin{pmatrix}-\cos\theta\\0\\\sin\theta\end{pmatrix}, \tag{7}$$

with the vacuum impedance $Z_0 = 1/\varepsilon_0 c = 377\ \Omega$. The emitted wave traveling towards the metal surface (6) is reflected off the latter leading in turn to an additional contribution of (7) to the local driving field. The first term in the Green's-function (A2) of Ref. 30 gives the local field distribution field caused by the space charge in the vacuum

$$\vec{E}_{\text{space}}^{\text{3D}}(x,y,z,t) = -\begin{pmatrix} 0 \\ 0 \\ 1 \end{pmatrix} \frac{1}{\varepsilon_0} \int_z^\infty n_{\text{vac}}\left(z', t - \frac{x}{c}\sin\theta\right) dz'$$

$$= E_{\text{space}}\left(z, t - \frac{x}{c}\sin\theta\right) \begin{pmatrix} 0 \\ 0 \\ 1 \end{pmatrix}. \tag{8}$$

In contrast to Brunel's model,[27] Eq. (8) does not lead to a vanishing electric field at the metal-vacuum interface because typically the major part of the electric field decay occurs within the metal with a decay length on the order of the Thomas-Fermi screening length of $\approx 0.1\ \text{nm}$. A typical situation ($\theta = 45°$ and $\lambda = 800\ \text{nm}$) is shown in Fig. 3(c) where the electric field distributions $E_\perp(z)$ and $E_\parallel(z)$ are plotted along the coordinate z. The black line shows the situation at low electric fields, i.e., without any space charge in the vacuum. At higher electric fields, $E_\perp(z)$ (red line) decays due to both space charge within the metal and that of the emitted electrons into the vacuum. In contrast, the electric field parallel to the surface $E_\parallel(z)$ (blue dashed line) decays in the metal within the skin depth and shows in vacuum a standing wave out of phase with that of $E_\perp(z)$. The green line sketches the "Brunel" model, i.e., $E_\perp(z)$ vanishes exactly at the metal-vacuum interface $z = 0$.

All physical quantities in Eqs. (1)–(8) do not depend on the y-coordinate and the x-coordinate which occurs exclusively in the combination $t' = t - (x/c)\sin\theta$. In the latter moving frame of reference all quantities do not depend on the x-coordinate either. Thus, we have found for our beam propagation geometry the effective 1D-dimensional equations of motion for the electric fields, charge density, and currents involved. Since we already restricted the motion of electrons to the z-direction it makes sense to consider the z-component of the involved electric fields only. The local electric field acting on the electrons in the vacuum (i.e., $z \geq 0$) is the sum of all fields in z-direction

$$E_{\text{loc}}(z,t) = \left[E_{\text{in}}(z,t) + E_{\text{re}}(z,t)\right]\sin\theta + \left[E_{\text{em(in)}}(z,t) + E_{\text{em(re)}}(z,t)\right]\sin\theta + E_{\text{space}}(z,t), \tag{9}$$

$$\frac{dp_i}{dt} = -e_0\, E_{\text{loc}}(z_i,t)\,\Theta(z_i). \tag{10}$$

It is important to note that Eqs. (1)–(10) fulfill the energy conservation of light matter interaction exactly, i.e., the energy per unit area deposited in the matter equals that missing in the reflected beam relative to that of the incident beam

$$\frac{1}{A}\sum_{i=1}^N \int_{-\infty}^\infty dt\, \delta[t - t_i(z_i = 0)]\left(c\sqrt{p_i(t)^2 + m_e^2 c^2} - m_e c^2\right) + \varepsilon_0 c \int_{-\infty}^\infty dt\left[1 - |r_{\text{p}}(\lambda,\theta)|^2\right]\cos\theta$$

$$\times\, |E_{\text{in}}(\infty,t) + E_{\text{em(in)}}(\infty,t)|^2 = \varepsilon_0 c \int_{-\infty}^\infty dt\,\cos\theta \times \left\{|E_{\text{in}}(\infty,t)|^2 - |E_{\text{re}}(\infty,t) + E_{\text{em(re)}}(\infty,t)|^2\right\}. \tag{11}$$

The first term of (11) is the kinetic energy of the electrons just after re-entrance into the metal, i.e., at time $t_i(z_i = 0)$. The second term is the thermal energy deposited within the skin depth of the metal according to the complex Fresnel coefficient $r_{\text{p}}(\lambda, \theta)$. In Fig. 3(b), we show that the deposited thermal energy per unit area is typically on the order of a few percent of the incident beam and will be neglected in the following by assuming a perfect conductor, i.e., $r_{\text{p}}(\lambda, \theta) = 1$.

In numerical calculations, the re-emitted electric field according to (6) and (7) leads to non-Markovian equations of motion for the electron positions z_i and momenta p_i because the entire history of current density determines the light field emitted by the electrons at time t. Setting $r_p(\lambda, \theta) = 1$ corresponds to $\Phi[r_p(\lambda, \theta)] = 0$ and removes the last term in the time argument of vacuum current in (7). Setting additionally $|z - z'| \cos\theta \approx 0$ and $(z + z') \cos\theta \approx 0$ in the time argument of vacuum current of (6) and (7) [and consequently $z \cos\theta \approx 0$ in (1) and (2)] results in a set of Markovian equations of motion (i.e., without retarded memory effects) for Eqs. (1)–(10). We justify this approximation with the following argument.

The largest electric fields perpendicular to the metal surface [Fig. 3(a)] are obtained for large θ. In this case, the wave vector $k_z = (\omega/c) \cos\theta$ of the standing wave along the z-coordinate is very small, i.e., in the vicinity of the metal surface, the electric field variations due to the standing wave can in good approximation be neglected relative to those created by the space charge in both metal and vacuum or the skin depth of the penetrating wave [Fig. 3(c)]. In the $z = 0$, $z' = 0$ approximation, the transversal electric fields do not depend any longer on the spatial coordinate of the electron which leads to the following modified expression for the local field:

$$E_{\text{loc}}^{\text{approx}}(z, t) = [E_{\text{in}}(0, t) + E_{\text{re}}(0, t)] \sin\theta + [E_{\text{em(in)}}(0, t) + E_{\text{em(re)}}(0, t)] \sin\theta + E_{\text{space}}(z, t). \quad (12)$$

In Eq. (12), exclusively the dynamic space charge $E_{\text{space}}(z, t)$ causes a position dependent driving force (10) for the electrons in the vacuum. This modification neither destroys the $t' = t - (x/c) \sin\theta$ symmetry of the problem nor does it violate the energy conservation of light-matter interaction [Eq. (11)].

B. Field-induced extraction of electrons from the metal target

The generation rate of vacuum electrons tunneling from the metallic target through a barrier is defined by the WF of the metal and the electric light field. In typical experiments, the electric fields due to the standing wave created by incident and reflected waves have values between 10^{11} and 10^{12} V/m or hundred to thousand volts per nanometer [Fig. 4]. At such high electric fields, various tunneling models (a recent review of such models can be found in Ref. 2) predict a transmission probability of electrons from $T_{\text{tunnel}}(100 \text{ V/nm}) \approx 0.1$ up to T_{tunnel} $(E_{\text{loc}} > 1000 \text{ V/nm}) \approx 1$ through the triangular barrier [Fig. 2(d)]. We calculated the transmission probability $T_{\text{tunnel}}(E_{\text{loc}})$ for copper by means of the Wentzel-Kramers-Brillouin (WKB) approximation the result of which is shown in Fig. 4(a). The transmission coefficient $T_{\text{tunnel}}(E_{\text{loc}})$ is essentially determined by the work function [WF in Fig. 2(c)] of the metal. In our calculations we take $WF = 5$ eV for copper. For calculating the maximum generation rate F_{max} of free electrons with $T_{\text{tunnel}}(E_{\text{loc}}) = 1$, we approximated the conduction band electrons of copper as a degenerate free electron gas with the Fermi velocity v_F and a density equal to the atomic density $n_e = \rho_{\text{Cu}} = 8.47 \times 10^{22} \text{ cm}^{-3}$ in a copper crystal

$$F_{\text{max}} = \frac{3}{16} \rho_{\text{Cu}} v_F \approx 2.5 \times 10^{34} \text{ e}^- \text{ s}^{-1} \text{ m}^{-2}. \quad (13)$$

The electron density and Fermi velocity are characteristic for the particular metal and independent of the driving laser source. The extraction of electrons from the metal is organized in our model calculations as follows. We start with an ensemble of N electrons each having a vanishing momentum $p_i = 0$ and initially residing at $z_i = -0.1$ pm within the metal. Due to the spatial positions, the local field in the vacuum (10) does not act on such electrons directly. In each time step Δt, we calculate the probability for the emission of an electron into the vacuum with the help of

$$P_{\text{emission}}(t) = F_{\text{max}} A \Delta t T_{\text{tunnel}}[E_{\text{loc}}(0, t)]. \quad (14)$$

At this point, the normalization area A comes into play which was introduced in the equations for the charge density (3) and current density (4) in the vacuum. In order to avoid numerical
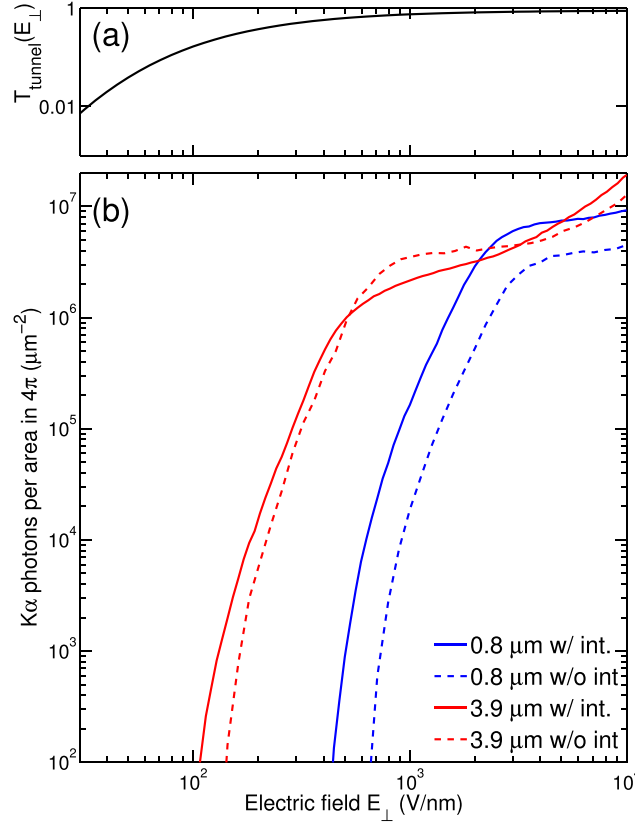
FIG. 4. (a) Electron extraction probability due to quantum mechanical tunneling as a function of the electric field amplitude perpendicular to the metal surface $E_\perp = E_{in}|1 + r_p(\lambda, \theta)|\sin(\theta)$. (b) Generated x-ray flux per surface area, i.e., Kα photons into solid angle $4\pi/\mu m^2$ as a function of $E_\perp$ for a 50 fs driver pulse at $\lambda = 0.8\,\mu m$ (blue curves) and an 80 fs pulse at $\lambda = 3.9\,\mu m$ (red). The curves labeled "without interaction" (dashed lines) are calculated by neglecting both the space charge due to electrons in the vacuum and the radiation reaction field. The latter allows for radiative damping and results in the correct energy conservation in the light-matter interaction. The solid lines labeled "with interaction" include the space charge in the vacuum.

artefacts, the product $A \cdot \Delta t$ has to be chosen in such a way that the emission probability $P_{emission}(t) < 0.1$ is small throughout the experiment. Depending on both $P_{emission}(t)$ and a random number, the electron i is emitted into the vacuum by a sudden change of $z_i = -0.1$ pm to $z_i = +0.1$ pm without changing its momentum $p_i = 0$. In this concept, the number of contributing electrons N is undetermined at the beginning of the experiment since the local field $E_{loc}(0, t)$ is not known beforehand.

It is important to note that the resulting space charge $n_{vac}^{3D}(x, y, z, t)$ and the electric field E_{space} originating from it depend critically on the cycle/wavelength of the optical driving field. The relevance of the space charge field for Kα generation can be estimated by considering F_{max} during an optical half cycle

$$E_{space}^{estimate}(\lambda) \approx \frac{F_{max}\, e_0}{\varepsilon_0}\frac{\lambda}{2c}. \tag{15}$$

For a driver wavelength of 800 nm, one estimates a value of $E_{space}^{estimate}(800\,nm) = 600\,V/nm$, much smaller than typical amplitudes of the optical field of several thousands of V/nm. As a consequence, the space charge has a negligible influence on the electron extraction for short wavelengths. For long wavelengths, however, $E_{space}^{estimate}(5000\,nm) = 3800\,V/nm$ influences electron extraction and, thus, x-ray generation strongly.

The "Brunel"-model[27] is a limiting case of our theory. Setting $WF = 0$ (i.e., neglecting any barrier) and using an arbitrarily high electron density in the metal the generation rate diverges

($F_{max} \rightarrow \infty$), i.e., the metal becomes a non-saturable reservoir of electrons. Neglecting in this limit the radiation reaction field [Eqs. (6) and (7)] corresponds exactly to the theory presented by Brunel. For typical electric fields applied in experiments, the infinite generation rate $F_{max} \rightarrow \infty$ leads to unrealistically high space charge densities [Eq. (8)] in the vacuum, i.e., $n_{vac}(z, t) \gg n_{metal}$. Furthermore, the missing radiation reaction field allows for an unrealistically high absorption of 20%–80% of the incoming photon flux [cf. Fig. 2(a) of Ref. 27] in the sub-100 fs time regime in which no highly ionized plasma has formed yet.

C. Deceleration of electrons and K-shell ionization within the metal target

After re-entering the metal target, the accelerated electrons do not experience the electric field of the laser anymore and are decelerated by energy loss mechanisms within the metal. Overall, K-shell ionization of target metal atoms plays only a minor role for the energy loss. In Fig. 5(a), we plot the cross section σ_K for K-shell ionization in copper as a function of electron energy.[33] When multiplying this cross section with the density of copper atoms in the target one finds $\sigma_K(300 \, keV) \, \rho_{Cu} = (600 \, \mu m)^{-1}$, i.e., only a small part of all accelerated electrons create a hole in the K-shell of Cu atoms in a $20 \, \mu m$ thick copper layer, a metal tape target typically used in experiments. The ratio of Cu Kα photons generated per electron is shown as a function of the kinetic electron entrance energy W_e in Fig. 5(b) for different angles of incidence (solid lines). Around an electron energy of 150 keV this ratio first saturates and then decreases, because the electrons start to be transmitted through the Cu tape. Between 20 keV and 200 keV, the ratio follows approximately $(W_e \, /900 \, keV)^2$ (dashed line) showing the importance of high
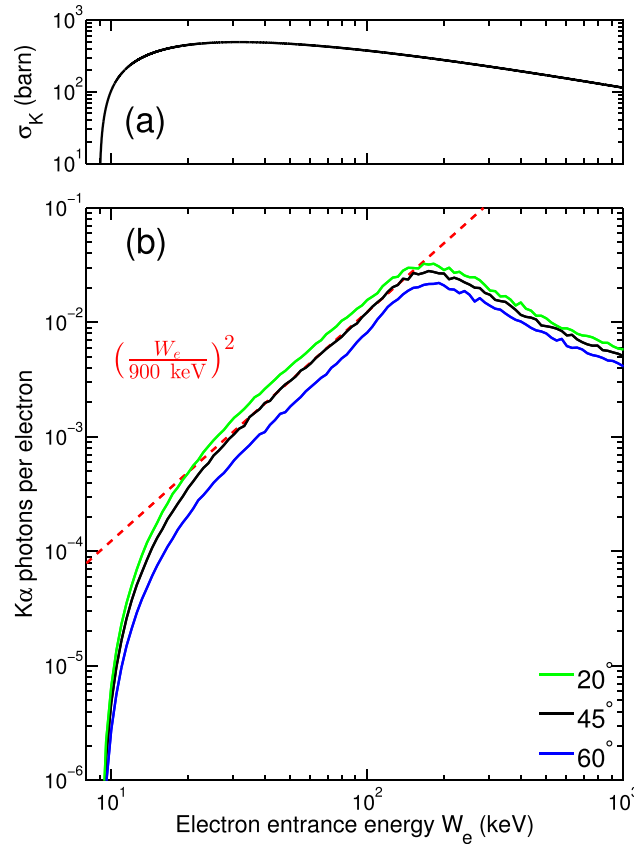

FIG. 5. (a) Cross section σ_K for K-shell ionization in copper as a function of the electron energy ($1 \, b = 10^{-24} \, cm^2$). (b) Calculated ratio Cu Kα photons/electron (solid lines) for a $20 \, \mu m$ thick Cu tape as a function of the electron entrance energy W_e for different angle of incidence θ as indicated. The dashed line shows that between 20 keV and 200 keV the ratio follows approximately $(W_e/900 \, keV)^2$.

energy electrons for efficient X-ray generation. The deceleration trajectories in the metal target, including K-shell ionization processes, are a material property and independent of the driving laser source.

K-shell ionized target atoms emit characteristic X-rays by filling their core holes with outer-shell electrons. The (spontaneous) characteristic emission covers a solid angle of 4π. The core hole lifetimes are of the order of a few femtoseconds, and thus, the duration of the generated hard X-ray bursts is determined by the much longer duration of the driving laser pulses and electron traveling time along the deceleration trajectories in the target.

In our theory, the electron target interaction which results in the K_α and Bremsstrahlung emission was calculated using a Monte Carlo method.[34] For the K-shell ionization cross section, we use the semiempirical formula introduced by Ref. [35], for the stopping power data from NIST[36] and for the Bremsstrahlung spectrum the Bethe-Heitler formula. We also included reabsorption of x-ray photons within the copper tape. Since we use only the $K\alpha$ photons emitted in the forward direction (the direction of the driving laser) in time-resolved experiments, the reabsorption of x-ray photons within the copper tape depends also on the angle of incidence θ as shown in Fig. 5(b).

Treating the electron-target interaction as a separate step in the model allows for calculating the number of emitted $K\alpha$ photons in a certain experimental geometry from a known energy distribution of re-entering electrons and the results shown in Fig. 5(b).

D. Beam profile of the driving laser

The equations of motion (1)–(14) give the energy distribution $ED(W_e)$ of electrons (W_e: electron energy) reentering the target for an arbitrary incident pulse $E_{in}(t)$ with plane phase fronts [cf. Eq. (1)] hitting the metal target under an angle of incidence θ

$$ED(W_e) = \frac{1}{A} \sum_{i=1}^{N} \int_{-\infty}^{\infty} dt \, \delta[t - t_i(z_i = 0)] \times \delta\left(c\sqrt{p_i(t)^2 + m_e^2 c^2} - m_e c^2 - W_e\right). \quad (16)$$

Together with the results shown in Fig. 5(b), we can now calculate the number of emitted $K\alpha$ photons per unit surface area with the help of the functional

$$K_\alpha[E_{in}^0 \cdot e_{in}(t), \theta], \quad (17)$$

where we have split the input field into an amplitude E_{in}^0 and a normalized time-dependent function $e_{in}(t)$. In a real experiment, there are no input pulses with infinitely broad plane wave fronts but typically a gaussian beam profile on the metal target. Thus, for a comparison with experiments we have to integrate over the beam profile

$$K_\alpha^{\text{beam}}[E_{in}(t), \theta, d_{\text{FWHM}}] = \int_{-\infty}^{\infty} dx \int_{-\infty}^{\infty} dy \times K_\alpha\left[E_{in}^0 \exp\left(-2\ln 2 \cdot \frac{x^2 \cos^2\theta - y^2}{d_{\text{FWHM}}^2}\right) \cdot e_{in}(t), \theta\right], \quad (18)$$

with d_{FWHM} being the full width at half maximum (FWHM) of the intensity profile of the driving laser. To be independent of the focusing conditions, we define

$$K_\alpha^{\text{gauss}}[E_{in}(t), \theta] = K_\alpha^{\text{beam}}[E_{in}(t), \theta, d_{\text{FWHM}}] \times \left[\int_{-\infty}^{\infty} dx \int_{-\infty}^{\infty} dy \exp\left(-2\ln 2 \cdot \frac{x^2 \cos^2\theta - y^2}{d_{\text{FWHM}}^2}\right)\right]^{-1}, \quad (19)$$

which gives the amount of $K\alpha$ photons per unit surface area for a gaussian beam profile of the driving laser.

III. RESULTS AND COMPARISON WITH EXPERIMENTAL DATA

We now discuss key results of our theoretical model. First, acceleration trajectories $z_i(t)$ of electrons in the vacuum are presented for different experimental conditions, followed by a detailed discussion of how the energy distribution of reentering electrons depends on the ensemble of trajectories. In addition to the dependence on the electric field amplitude E_{in}^0, the driver wavelength λ, and the angle of incidence θ, we consider the response to very short electric field transients having an identical spectrum but different carrier-envelope phases ϕ_{cep}. Thereafter, we analyze the time structure of the generated hard x-ray pulses. Finally, the generated flux of Kα photons is calculated for driving pulses with gaussian beam profiles [Eqs. (18) and (19)] and compared with experimental results.

A. Acceleration trajectories of electrons in the vacuum and energy distribution of reentering electrons

After its "birth" in vacuum, a free electron is accelerated in the first half cycle of the electric field of the driving pulse and smashed back into the metal target in the next half cycle of opposite sign. The trajectory depends sensitively on the phase of electron birth within the optical cycle. In the case of negligible space charge, the electrons generated in the first quarter of the optical cycle do not enter the metal target at later times. Starting with phase $\phi = \pi/2$ the electron enters the metal target with an additional amount of energy (solid line in Fig. 3(a) of Ref. 21). Electron birth within the phase range from $\phi = \pi$ to 2π creates no accelerated electrons since the electric field points into the wrong direction. In Fig. 4(b), we show the generated x-ray flux per surface area, i.e., Kα photons into solid angle $4\pi/\mu m^2$ as a function of the electric field perpendicular to the surface $E_\perp$ for driver pulses with a center wavelength and pulse duration as indicated. The respective dashed curves labeled "without interaction" are calculated by neglecting both the space charge due to electrons in the vacuum [Eq. (8)] and their radiation reaction field [Eqs. (6) and (7)]. The two dashed curves in Fig. 4(b) are of similar shape and essentially shifted along the logarithmic x-axis by the ratio squared of the two wavelengths, confirming the $I \times \lambda^2$ rule empirically found in recent experiments.[21] The so-called vacuum heating of free electrons in the electric field of the driving pulses,[1,27] i.e., electron acceleration, represents a key step of the generation scheme. At a fixed electric field strength, one expects higher kinetic energies of accelerated electrons for a longer acceleration period in time, corresponding to a longer optical period or wavelength λ of the driving pulse. The red dashed line for $\lambda = 3.9\,\mu m$ in Fig. 4(b) is somewhat steeper at low electric fields $E_\perp$ because the finite tunneling barrier [Fig. 2(d)] leads to a reduced extraction rate at low fields [Fig. 4(a)].

The solid lines in Fig. 4(b) labeled "with interaction" were calculated including the space charge due to electrons in the vacuum [Eq. (8)] and their radiation reaction field [Eqs. (6) and (7)]. At short driver wavelengths ($\lambda = 800\,nm$, blue solid line), the x-ray generation sets in at lower electric fields $E_\perp$ and reaches a higher value of saturation compared to its counterpart without interaction (blue dashed line). The result for $\lambda = 3.9\,\mu m$ (red solid line) shows a similar behavior with an additional pronounced dip around field strengths of $E_\perp \approx 800\,V/nm$. The origin of the latter is the space charge of vacuum electrons [Eq. (8)] having its strongest influence at intermediate field strengths. At low electric fields, space charge effects are absent as the tunneling barrier [Fig. 2(d)] limits the density of vacuum electrons to a small value. At extremely high electric fields $E_\perp$ such as in experiments with $\lambda = 800\,nm$ drivers (cf. blue curves), the extraction rate saturates [cf. Eq. (14)] and leads to the scenario discussed in Fig. 3(c). For intermediate field strengths $E_\perp \approx 800\,V/nm$ (red line) $E_\perp(z)$ decays due to both space charge within the metal and the space charge of the vacuum electrons. For even higher field strengths, however [black line in Fig. 3(c)], the decay of $E_\perp(z)$ is again dominated by the space charge in the metal [black line in Fig. 3(c)].

The electric field due to the space charge in vacuum [Eq. (8)] has different effects on electron extraction and acceleration. A large space charge during the phase of electron extraction reduces the extraction rate [Eq. (14)] because $\vec{E}_{space}$ [Eq. (8)] points into the direction opposite to $\vec{E}_\perp = \vec{E}_{in} + \vec{E}_{re}$ [Eqs. (1) and (2)]. In contrast, during the phase of electron acceleration

towards the metal surface, $\vec{E}_{\text{space}}$ and $\vec{E}_{\perp}$ add up leading to higher kinetic energies of the re-entering electrons. The latter effect dominates for short driver wavelengths [$\lambda = 800$ nm: blue solid line in Fig. 4(b)], whereas the reduced extraction rate is important for long driver wavelengths [$\lambda = 3.9\,\mu$m: red solid line in Fig. 4(b)].

In Fig. 6(a), we plot the trajectories of electrons in the strong electric field of a p-polarized 50 fs pulse centered at $\lambda = 5\,\mu$m (thick solid line) and reflected from a copper target under an angle of $\theta = 45°$. The electric field amplitude was $E_{\text{in}} = 200$ V/nm. In Fig. 6(b), we show the corresponding distribution of entrance energies W_e at the metal surface (green curve). The individual trajectory depends sensitively on the phase of electron birth within the optical cycle and the space charge field makes all electrons return to the target independent of the time of their "birth."

In order to gain a deeper insight into the extraction and acceleration mechanisms, we calculated the trajectories and corresponding distributions of entrance energies W_e for an extremely
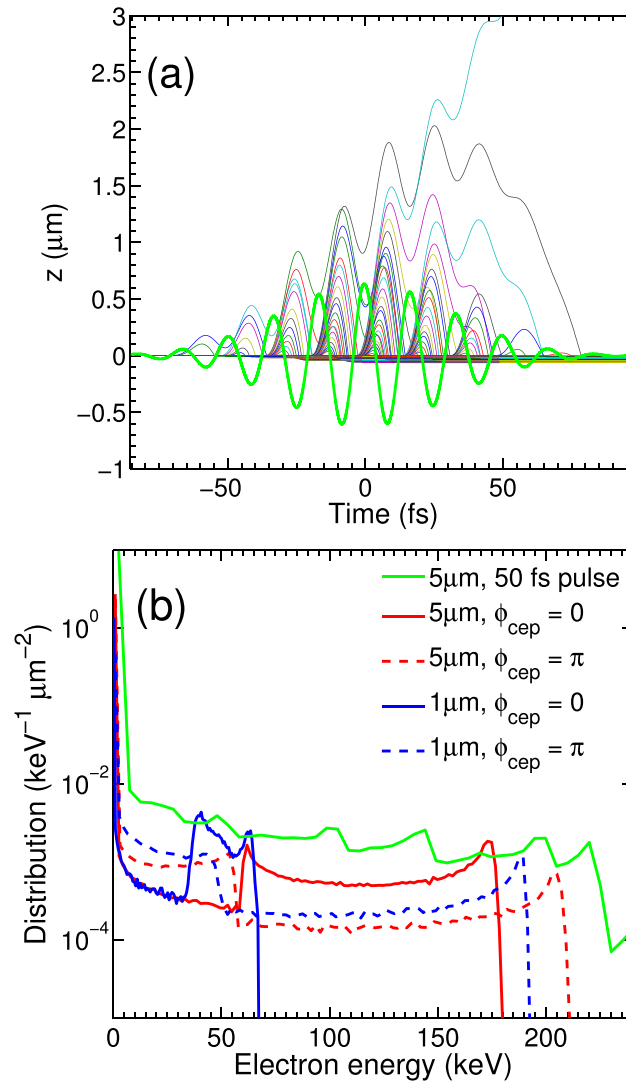

FIG. 6. Electron acceleration in the strong electric field of a p-polarized femtosecond laser pulse being reflected from a metal target under an angle of incidence of $\theta = 45°$. (a) Electron trajectories in the vacuum for a 50 fs pulse (thick solid line) at $\lambda = 5\,\mu$m with an amplitude of $E_{\text{in}} = 200$ V/nm: the individual trajectory depends sensitively on the phase of electron birth within the optical cycle. (b) Green solid line: corresponding distribution of entrance energies W_e at the metal surface. Red and blue curves: distributions of entrance energies for extremely short pulses (thick solid and dashed lines in Fig. 7) for carrier-envelope phases as indicated.

short pulse for different carrier-envelope phases ϕ_{cep}. The trajectories are shown in Figs. 7(a)–7(d), the corresponding energy distributions in Fig. 6(b), and the generated x-ray flux per surface area in Fig. 8. In addition, we show in Fig. 7(e) the spatial profiles of the electric field due to space charge $E_{space}(z, t = 0)$ for the different situations. The table in the inset shows the wavelength λ, carrier-envelope phase ϕ_{cep}, and the respective electric field at time zero $E_{\perp}(t = 0)$. The trajectories for $\lambda = 5\,\mu m$ [Figs. 7(a) and 7(b)] clearly demonstrate the space charge effect on the electron extraction process. A high local driving field during the extraction process is favorable for overcoming the counterproductive action of the space charge. At the much shorter wavelength $\lambda = 1\,\mu m$, we observe the opposite dependence on the carrier envelope phase ϕ_{cep} [Figs. 7(c) and 7(d)]. Here, the electron extraction is almost independent of the space charge because of the high driver fields. For short driver wavelengths, it is more important to have a large field during the phase of electron acceleration towards the metal surface since the electric field due to the space charge in vacuum (8) adds to $\vec{E}_{\perp} = \vec{E}_{in} + \vec{E}_{re}$, resulting in higher kinetic energies of the reentering electrons.

We summarize this behavior in Fig. 8 where panel (a) displays the x-ray flux generated per surface area with a mono-cycle pulse as a function of both the driver wavelength λ and the carrier-envelope phase ϕ_{cep}. The generated number of Kα photons into a solid angle of 4π per μm^2 is shown for various driver wavelengths λ in panel (b).
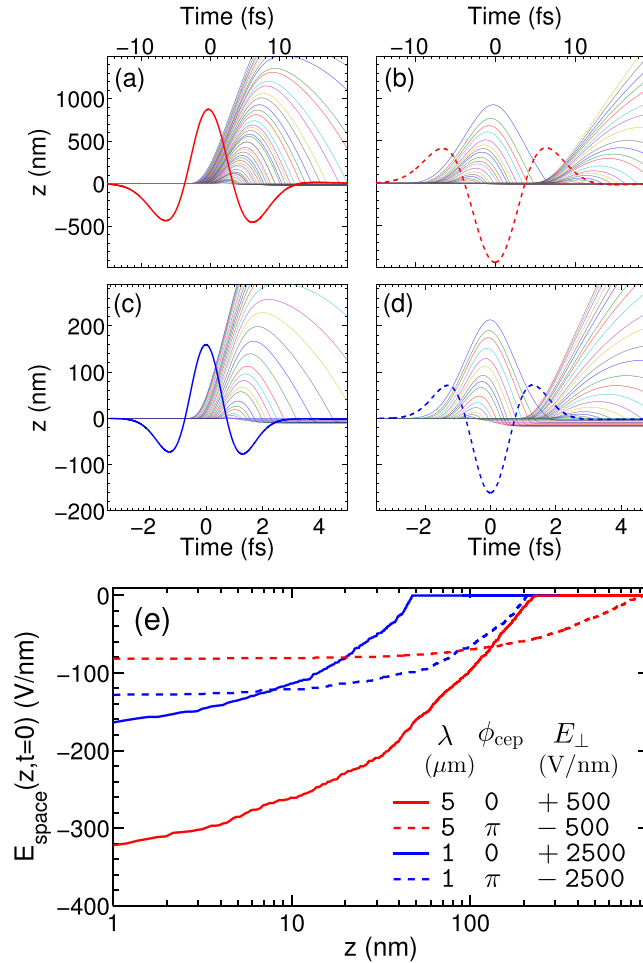

FIG. 7. (a) and (b) Electron trajectories for an extremely short pulse at $\lambda = 5\,\mu m$ (thick solid and dashed lines) for two different carrier-envelope phases. (c) and (d) Corresponding trajectories for $\lambda = 1\,\mu m$. (e) Spatial profiles of the electric field due to space charge $E_{space}(z, t = 0)$ [Eq. (8)]. The table shows for the different situations [panels (a)–(d)] the wavelength λ, carrier-envelope phase ϕ_{cep}, and electric field at time zero $E_{\perp}(t = 0)$.
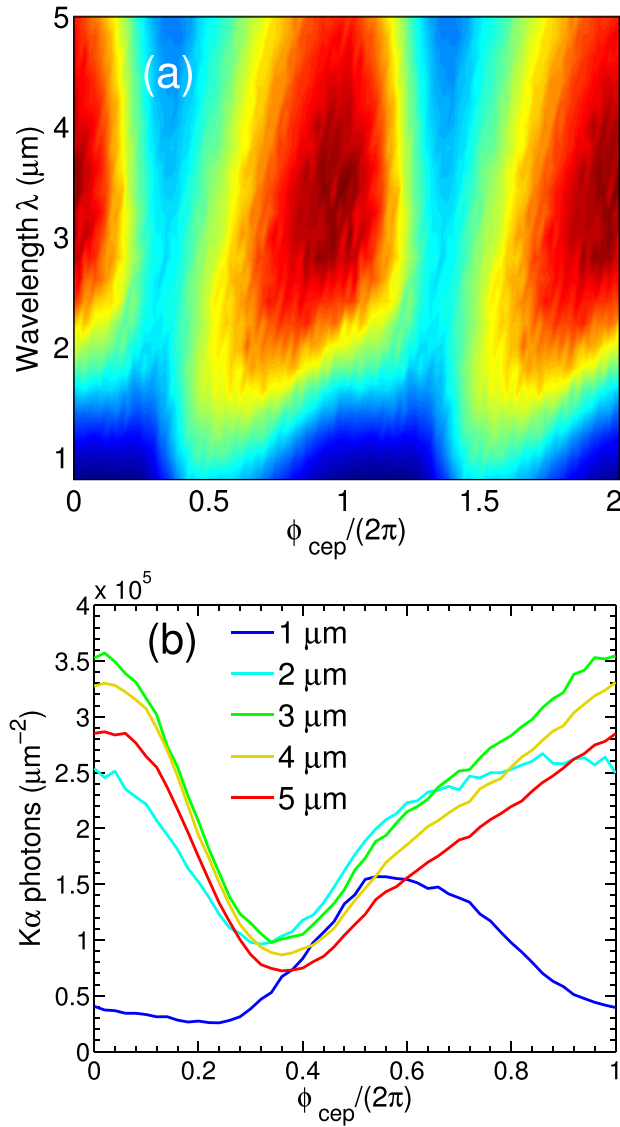
FIG. 8. (a) Contour plot of the generated x-ray flux per surface area for an extremely short mono-cycle pulse [cf. trajectories in Fig. 7 and distributions in Fig. 6(b)] as a function of both the driver wavelength λ and the carrier-envelope phase ϕ_{cep}. (b) Sections of the contour plot for various driver wavelengths λ as indicated.

B. Duration of the generated Kα pulses

The pulse duration of the generated Kα pulses is determined by various factors. Certainly, the pulse duration of the optical driver pulse sets a lower limit for the temporal profile of the distribution of energetic electrons reentering the metal tape [Eq. (16)]. Thus, one expects the shortest Kα pulses for driver pulses as shown in Fig. 7. For such short pulses, the deceleration trajectories of electrons within the metal target discussed in Sec. II C represent the dominant contribution to the Kα pulse duration. Here, the shortest Kα pulses are expected in forward direction, the propagation direction of the driver laser [incoming beam in Fig. 1] because the projection of electron velocity onto this direction is maximum. The overall traveling time of electrons and, consequently, the period over which x-rays are generated, increases with the target thickness. The lifetime of the core hole in ionized Cu atoms of a few femtoseconds is short compared to the traveling time of electrons through the target and has a negligible influence on the time structure of the generated characteristic x-rays.

In Fig. 9, we present calculated temporal profiles for a $20\,\mu m$ thick Cu target illuminated under $\theta = 45°$. The solid line in panel (a) shows the calculated temporal profile of the Kα radiation generated by a 50-fs long pulse at $\lambda = 800\,nm$ with an electric field amplitude of $E_\perp = 3300\,V/nm$. Such parameters correspond to the experimental situation of Ref. 5 where field-induced quasi-instantaneous inter-ionic charge transfer has been studied in crystalline LiH. The integrated charge change $\Delta Q(t)$ around the H-atom [Fig. 2(e) of Ref. 5] is shown in Fig. 9(a) (symbols) and follows the cross-correlation of a sub-50 fs optical pulse with the Kα pulse. We find excellent agreement of the calculated with the measured duration of Kα pulses. In panel (b), we plot the calculated temporal profile of the Kα pulse generated by a 80-fs long pulse at $\lambda = 3.9\,\mu m$ with an electric field amplitude of $E_\perp = 600\,V/nm$. (experiment in Ref. 21). The somewhat longer Kα pulse duration is essentially due to the longer mid-infrared driver pulse.

C. Angle dependence of x-ray yield

Recent experiments with femtosecond driver pulses centered at $\lambda = 3.9\,\mu m$ have revealed a pronounced change of the generated copper Kα flux with the angle of incidence on the target θ [symbols in Fig. 10(b), Ref. 21]. On the one hand, the electric field amplitude perpendicular to the metal surface $E_\perp = E_{in}|1 + r_p(\lambda, \theta)|\sin(\theta)$ [Fig. 3(a)] increases with $\sin\theta$. On the other hand, the illuminated area on the metal target increases with $1/\cos\theta$ [(18)] when neglecting diffraction effects. To get beyond such simple geometric arguments which are in conflict with energy conservation at large θ, we calculated the absorption of the driver field in the target as a function of the angle of incidence θ of an 80-fs pulse at $\lambda = 3.9\,\mu m$ (electric field amplitude of $E_{in}^0 = 500\,V/nm$) for two different scenarios. In Fig. 10(a), the red line shows a calculation without radiative damping and space charge [Eqs. (6)–(8)]. For $\theta > 70°$, energy conservation is violated since more infrared photons are absorbed than contained in the incident beam. A calculation including radiative damping and space charge (black line) accounts correctly for energy conservation in light-matter interaction. Here, absorption saturates at about $\approx 60\%$. With radiative damping [Eqs. (6) and (7)] the electric field re-emitted by the space charge electrons interferes destructively with the reflected beam so that energy conservation is fulfilled according to Eq. (11). In Fig. 10(b), we present the number of Kα photons per laser shot as a function of θ normalized to the red curve at $\theta = 59°$. According to theory, the space charge (black curve) enhances the Kα emission slightly for $\theta < 50°$ relative to the calculation without space charge
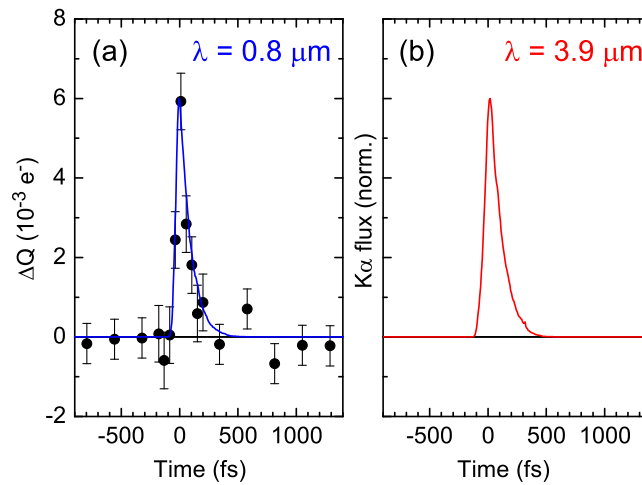

FIG. 9. (a) Solid line: calculated temporal profile of the Kα radiation generated by a 50-fs long pulse at $\lambda = 0.8\,\mu m$ with with an electric field amplitude of $E_\perp = 3300\,V/nm$. The symbols represent experimental results taken from Fig. 2(e) of Ref. 5 showing the quasi-instantaneous integrated charge change $\Delta Q(t)$ of crystalline LiH around the H-atom versus the delay time t occurring during the temporal overlap with a strong optical field. (b) Calculated temporal profile of the Kα radiation generated by a 80-fs long pulse at $\lambda = 3.9\,\mu m$ with with an electric field amplitude of $E_\perp = 600\,V/nm$.
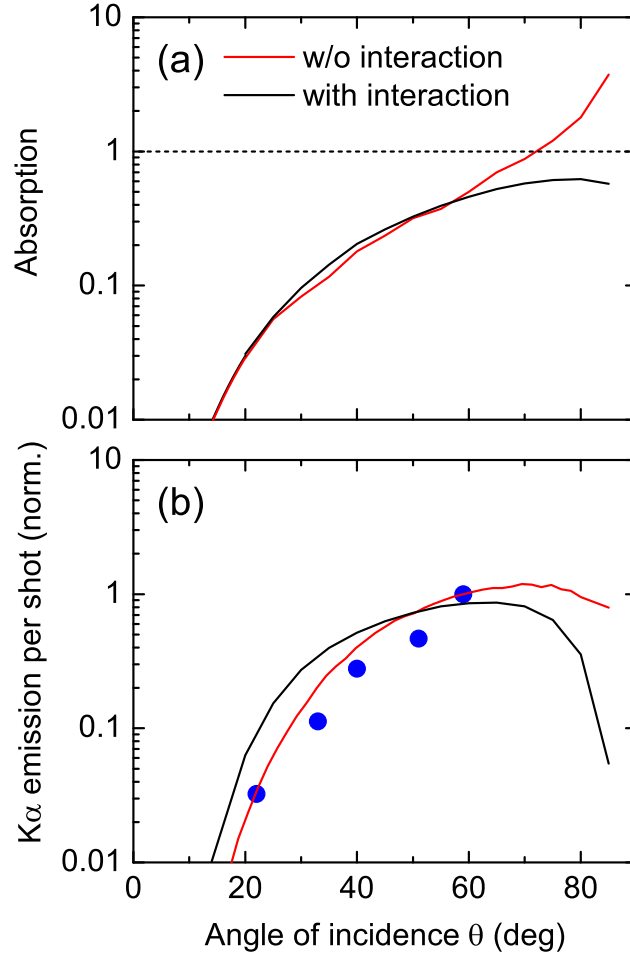
FIG. 10. (a) Absorption of the driver field as a function of the angle of incidence θ for an 80-fs long pulse at $\lambda = 3.9\,\mu m$ with an electric field amplitude of $E_{in}^{0} = 500\,V/nm$. The red line shows a calculation without space charge and radiative damping. The black line shows results of the full model. (b) Emitted Kα photons per laser shot as a function of θ normalized to the red curve at $\theta = 59°$. The symbols represent experimental results taken from Ref. 21.

and radiative damping (red curve). For $\theta > 70°$, the radiative damping terms of the full theory [Eqs. (6) and (7)] reduce the Kα emission significantly by attenuating the local field acting on the electrons [Eq. (12)].

D. Kα generation with gaussian beams

For a most direct comparison with experiment, we calculated the Kα flux generated by driving pulses with a gaussian beam profile [Eqs. (18) and (19)]. In Fig. 11, the generated x-ray flux per surface area, i.e., Kα photons into solid angle $4\pi/\mu m^2$ is plotted as a function of the electric field amplitude perpendicular to the surface (lines). Such curves were calculated with the same parameter set as in Fig. 4(b). Applying Eq. (19) leads to a smoothing of the latter curves since Eq. (18) corresponds to a convolution of the results in Fig. 4(b) with the gaussian beam profile.

The symbols in Fig. 11 represent experimental results from Ref. 21. Such data lie in-between the theoretical calculations including the space charge [Eq. (8)] and the radiation reaction field [Eqs. (6) and (7)] (solid lines) and those without the latter mechanisms (dashed lines). This comparison shows that the details of the quantum mechanical properties of the metal, i.e., the work function WF and the maximum extraction current density [Eq. (13)] have a significant influence on the amount of emitted Kα photons. The theoretical concept presented here focuses
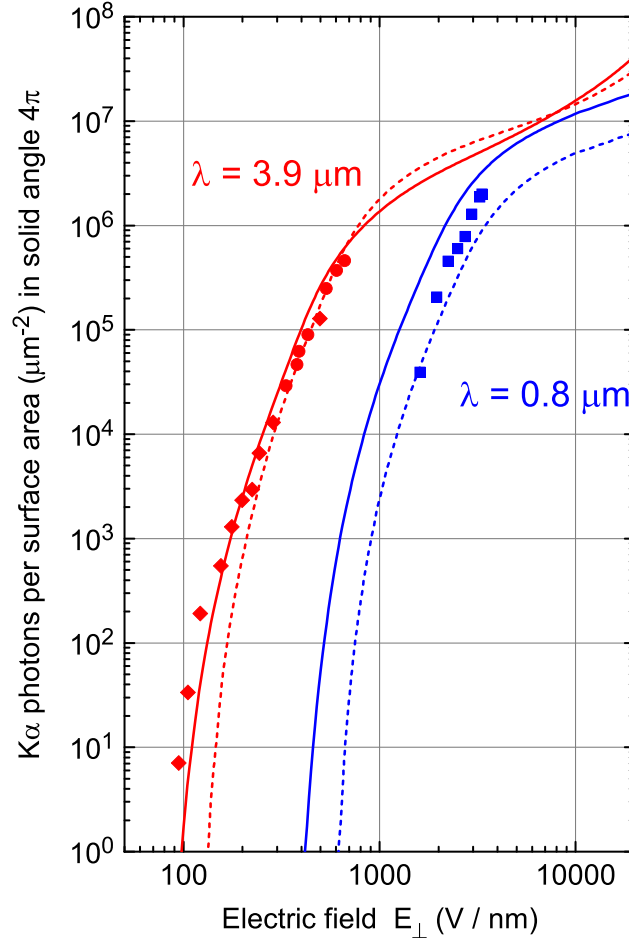
FIG. 11. Generated x-ray flux per surface area, i.e., Kα photons into solid angle $4\pi/\mu m^2$ for gaussian beam profiles calculated with help of Eq. (19) from the data already shown in Fig. 4(b). The symbols represent experimental data from Ref. 21.

on long driver wavelengths, large angles of incidence, and concomitantly "low" electric field strengths, i.e., the experiments with $\lambda = 3.9\,\mu m$ (red symbols). The overall agreement between theory and experiment is good and demonstrates that the physical picture presented here accounts for the key features of the x-ray generation process. Concerning the experiments with $\lambda = 0.8\,\mu m$ (blue symbols) we expect that plasma formation within the pulse duration begins to play an additional role in the x-ray generation scenario.

IV. CONCLUSIONS

In conclusion, we have presented a theoretical model for describing the physical processes which underlie hard x-ray generation with metal targets interacting with intense femtosecond optical pulses. Similar to Brunel's concept,[27] the light-metal interaction is treated with the linear Fresnel equations for electrons residing in the metal and the vacuum heating model is applied for electrons in the vacuum. In extension of Ref. 27, we invoke quantum mechanical tunneling for the extraction of electrons from the metal surface. This keeps the electron densities in the vacuum at realistic values which are—at any time—much smaller than the electron density in the target. Moreover, the radiation reaction field is included in an effective one-dimensional propagation geometry, thus allowing for radiative damping and the correct energy conservation in light-matter interaction. The generated flux of Kα photons is calculated as a function of the incident optical intensity I, driver wavelength λ, angle of incidence θ, and

carrier-envelope phase ϕ_{cep} of the driving pulses. The different parameters are set to values close to recent experiments.[21] We demonstrate that the theoretical model fully accounts for the experimental results. It reveals the key quantities governing the efficiency of the x-ray generation processes. In case of a negligible space charge in vacuum, the theory predicts a characteristic x-ray flux proportional to the incident intensity and the wavelength squared $I\,\lambda^2$, suggesting the application of mid-infrared driving pulses for a strong enhancement of the generated x-ray flux. For optimized focusing conditions, the space charge enhances slightly the x-ray flux for $\lambda < 3.5\,\mu$m and causes a gradual saturation at longer driver wavelengths. Such results will allow for designing a new generation of optically driven table-top sources for femtosecond hard x-ray pulses.

ACKNOWLEDGMENTS

[1] W. Priedhorsky, D. Lier, H. Day, and D. Gerke, "Hard-x-ray measurements of 10.6-μm laser-irradiated targets," Phys. Rev. Lett. **47**, 1661 (1981).

[2] S. V. Yalunin, M. Gulde, and C. Ropers, "Strong-field photoemission from surfaces: Theoretical approaches," Phys. Rev. B **84**, 195426 (2011).

[3] G. Herink, D. R. Solli, M. Gulde, and C. Ropers, Nature **483**, 190 (2012).

[4] J. Stingl, F. Zamponi, B. Freyer, M. Woerner, T. Elsaesser, and A. Borgschulte, "Electron transfer in a virtual quantum state of LiBH$_4$ induced by strong optical fields and mapped by femtosecond x-ray diffraction," Phys. Rev. Lett. **109**, 147402 (2012).

[5] V. Juvé, M. Holtz, F. Zamponi, M. Woerner, T. Elsaesser, and A. Borgschulte, "Field-driven dynamics of correlated electrons in LiH and NaBH$_4$ revealed by femtosecond x-ray diffraction," Phys. Rev. Lett. **111**, 217401 (2013).

[6] P. Bowlan, E. Martinez-Moreno, K. Reimann, T. Elsaesser, and M. Woerner, "Ultrafast terahertz response of multi-layer graphene in the nonperturbative regime," Phys. Rev. B **89**, 041408(R) (2014).

[7] C. Somma, K. Reimann, C. Flytzanis, T. Elsaesser, and M. Woerner, "High-field terahertz bulk photovoltaic effect in lithium niobate," Phys. Rev. Lett. **112**, 146602 (2014).

[8] C. Bressler and M. Chergui, "Ultrafast x-ray absorption spectroscopy," Chem. Rev. **104**, 1781–1812 (2004).

[9] A. Rousse *et al.*, "Femtosecond x-ray crystallography," Rev. Mod. Phys. **73**, 17–31 (2001).

[10] M. Bargheer, N. Zhavoronkov, M. Woerner, and T. Elsaesser, "Recent progress in ultrafast x-ray diffraction," Chem. Phys. Chem. **7**, 783–792 (2006) .

[11] C. Bostedt *et al.*, "Ultra-fast and ultra-intense x-ray sciences; first results from the Linac coherent light source free-electron laser," J. Phys. B **46**, 164003–164023 (2013).

[12] M. M. Murnane *et al.*, "Ultrafast x-ray pulses from laser-produced plasmas," Science **251**, 531–536 (1991).

[13] G. Korn, A. Thoss, H. Stiel, U. Vogt, M. Richardson, T. Elsaesser, and M. Faubel, "Ultrashort 1-kHz laser plasma hard x-ray source," Opt. Lett. **27**, 866–868 (2002).

[14] Y. Jiang, T. Lee, W. Li, G. Ketwaroo, and C. G. Rose-Petruck, "High-average-power 2-kHz laser for generation of ultrashort x-ray pulses," Opt. Lett. **27**, 963–965 (2002).

[15] C. Ziener *et al.*, "Optimization of Kα bursts for photon energies between 1.7 and 7 keV produced by femtosecond-laser-produced plasmas of different scale length," Phys. Rev. E **65**, 066411 (2002).

[16] N. Zhavoronkov, Y. Gritsai, G. Korn, and T. Elsaesser, "Ultra-short efficient laser-driven hard x-ray source operated at a kHz repetition rate," Appl. Phys. A **79**, 663–667 (2004).

[17] N. Zhavoronkov, Y. Gritsai, M. Bargheer, M. Woerner, T. Elsaesser, F. Zamponi, I. Uschmann, and E. Förster, "Microfocus CuK$_\alpha$ source for femtosecond x-ray science," Opt. Lett. **30**, 1737–1739 (2005).

[18] F. Zamponi *et al.*, "Femtosecond hard x-ray plasma sources with a kilohertz repetition rate," Appl. Phys. A **96**, 51–58 (2009).

[19] S. Fourmaux, C. Serbanescu, R. E. Kincaid, Jr., A. Krol, and J. C. Kieffer, "Kα x-ray emission characterization of 100 Hz, 15 mJ femtosecond laser system with high contrast ratio," Appl. Phys. B **94**, 569–575 (2009).

[20] F. Zamponi *et al.*, "Ultrafast large-amplitude relocation of electronic charge in ionic crystals," Proc. Natl. Acad. Sci. U.S.A. **109**, 5207–5212 (2012).

[21] J. Weisshaupt, V. Juve, M. Holtz, S. Ku, M. Woerner, T. Elsaesser, S. Alisauskas, A. Pugzlys, and A. Baltuska, "High-brightness table-top hard X-ray source driven by sub-100 femtosecond mid-infrared pulses," Nat. Photonics **8**, 927–930 (2014).

[22] M. Lewenstein, P. Balcou, M. Y. Ivanov, A. L'Huillier, and P. B. Corkum, "Theory of high-harmonic generation by low-frequency laser fields," Phys. Rev. A **49**, 2117–2132 (1994).

[23] W. Lu, M. Nicoul, U. Shymanovich, A. Tarasevitch, p. Zhou, K. Sokolowski-Tinten, D. von der Linde, M. Masek, P. Gibbon, and U. Teubner, "Optimized Kα x-ray flashes from femtosecond-laser-irradiated foils," Phys. Rev. E **80**, 026404 (2009).

[24] P. Gibbon *et al.*, "Modelling and optimisation of fs laser-produced Kα sources," Appl. Phys. A **96**, 23 (2009).

[25] D. von der Linde and H. Schüler, "Breakdown threshold and plasma formation in femtosecond laser-solid interaction," J. Opt. Soc. Am. B **13**, 216 (1996).

[26] P. Gibbon and E. Förster, "Short-pulse laser-plasma interactions," Plasma Phys. Controlled Fusion **38**, 769 (1996).

[27]F. Brunel, "Not so resonant, resonant absorption," Phys. Rev. Lett. **59**, 52–55 (1987).

[28]M. K. Grimes, A. R. Rundquist, Y.-S. Lee, and M. C. Downer, "Experimental identification of 'vacuum heating' at femtosecond-laser-irradiated metal surfaces," Phys. Rev. Lett. **82**, 4010 (1999).

[29]C. Rödel, M. Heyer, M. Behmke, M. Kübel, O. Jäckel, W. Ziegler, D. Ehrt, M. C. Kaluza, and G. G. Paulus, "High repetition rate plasma mirror for temporal contrast enhancement of terawatt femtosecond laser pulses by three orders of magnitude," Appl. Phys. B **103**, 295 (2011).

[30]I. Waldmüller *et al.*, Phys. Rev. B **69**, 205307 (2004).

[31]T. Shih *et al.*, Phys. Rev. B **72**, 195338 (2005).

[32]J. E. Sipe, "New Green-function formalism for surface optics," J. Opt. Soc. Am. B **4**, 481 (1987).

[33]D. Berenyi, G. Hock, S. Ricz, B. Schlenk, and A. Valek, J. Phys. B: At. Mol. Phys. **11**, 709 (1978).

[34]D. C. Joy, "An introduction to Monte Carlo simulations," Scanning Microsc. **5**, 329–337 (1991).

[35]X. Llovet *et al.*, "Measurements of K-shell ionization cross sections of Cr, Ni, and Cu by impact of 6.5–40 keV electrons," J. Phys. B: At. Mol. Opt. Phys. **33**, 3761–3772 (2000).

[36]J. H. Hubbell and S. M. Seltzer, "Tables of x-ray mass attenuation coefficients and mass energy-absorption coefficients," National Institute of Standards and Technology, 1996.